INTERNATIONAL JOURNAL FOR NUMERICAL METHODS IN FLUIDS, VOL. 22, 137–148 (1996)

VALIDATION OF A NAVIER–STOKES SOLUTION ALGORITHM WITH EXPERIMENTAL VALUES IN A SUPERSONIC WAKE

FRIEDRICH LEOPOLD

ISL, French–German Research Institute of Saint-Louis, 5 Rue du Général-Cassagnou, F-68301 Saint Louis, France

SUMMARY

This paper describes the validation of a finite element solver for an axisymmetric compressible flow with experimental values, especially velocities measured with a laser Doppler anemometer in the near wake of a circular cylinder. The equations under consideration are the Navier-Stokes equations with turbulent terms. A time-stepping scheme for the solution of these equations can be produced by applying a forward-time Taylor series expansion including time derivatives of second order. These time derivatives are evaluated in terms of space derivatives in the Lax–Wendroff fashion. The method is based on unstructured triangular grids with a high resolution in the radial direction. In order to predict the measured turbulent intensities more exactly, a modification of the Baldwin–Lomax model is necessary.

KEY WORDS: validation; Navier–Stokes equations; Taylor–Galerkin approach; finite elements; laser Doppler anemometry

1. INTRODUCTION

An accurate prediction of the flow behaviour around aircraft is of great importance for the development of new aerospace technologies. Therefore the prediction of aerodynamic behaviour is still hampered by our lack of knowledge concerning afterbody flows. As is well-known, the base drag of a projectile can reach up to 50% of the total drag at transonic or moderately high Mach numbers.[1] Owing to the great practical importance of base flows, many efforts have been devoted to this domain. Recent articles on such investigations were written by Delery and Lacau[2] in 1988 and Delery and Wagner[1] in 1990. In order to cut down the high costs involved in the development of aerospace technologies, the initial expensive wind tunnel experiments are increasingly being replaced by numerical simulations on computers. However, these methods are unsuitable for practical aerodynamic applications without validation. This subject will not be dealt with in greater detail from a general point of view, but the discussion will be limited to the examination of the near wake of a projectile in a supersonic flow. In order to obtain a suitable validation, a configuration in which the experimental set-up and the numerical simulation are very close to each other will have to be defined. It is advantageous to avoid the shock waves provoked by the projectile and their reflections due to the wind tunnel geometry in order to prevent their interaction with the wake. Therefore a rod is used and fixed in the stagnation chamber in order to avoid shocks which would be provoked by attaching the body in the supersonic part of the wind tunnel. Instead, the computational domain begins one diameter before the base, where the inflow boundary is a measured boundary layer profile. The validation of a numerical method takes several steps into account.[3]

1. The governing equations have to describe the flow conditions in a correct way. The wake flow is simulated with the compressible Navier–Stokes equations in an axisymmetric co-ordinate

CCC 0271–2091/96/020137–12

Received November 1993
Revised June 1994

system. The appearance of sub-, trans- and supersonic flow regions forces us to use the unsteady formulation.
2. In order to simulate complex configurations after the validation, the finite element method seems to be very useful. In the past several authors such as Löhner *et al.*[4] and Peraire *et al.*[5] proposed that finite elements should be applied to a Lax–Wendroff scheme.
3. Convergence and stability are very important for the accuracy of the results. The time steps have to be kept below a certain limit and artificial viscosity is added to damp overshoots or wiggles where the exact solution shows jumps.
4. In order to verify the numerical procedure, simple cases such as non-linear wave propagations in a shock tube are calculated and compared with the analytical solutions.[6]
5. Finally, the configuration chosen for the validation could be calculated and certain modifications, e.g. the turbulence model, were necessary in order to get a correct description of the flow field.

In the first part of this paper the configuration and flow conditions for this validation experiment are introduced. They are followed by a description of the experimental techniques, the method for the numerical simulation and finally the comparison between the experimental values and the theoretical investigations.

2. EXPERIMENTAL SET-UP

2.1. *Facilities*

All measurements have been carried out in the ISL blow-down wind tunnel. The compressed air is stocked in tubes under a pressure of 250 bar. The air is filtered and dried in order to prevent shocks from appearing in the nozzle due to the condensation of humidity at low temperatures. The pressure in the stagnation chamber is estimated at 4·25 bar for a Mach number $Ma = 2{\cdot}06$. The temperature in the chamber ranges from 10 to 30 °C. This leads to the following conditions in the test section: temperature $\bar{T}_\infty = 158\,K$, pressure $\bar{p}_\infty = 466\,hPa$, density $\bar{\rho}_\infty = 1\cdot022\,\mathrm{kg\,m^{-3}}$ and velocity $\bar{u}_\infty = 519{\cdot}1\,\mathrm{m\,s^{-1}}$. The time under constant flow conditions for a blow-down is about $40\,s$. The dimensions of the test section are $200 \times 200\,\mathrm{mm}^2$. The Reynolds number is $1{\cdot}9 \times 10^6$ based on the diameter of the cylinder (38·66 mm). The cylindrical body is fixed in the stilling chamber of the wind tunnel in order to suppress the shocks which would be provoked by attaching the body in the supersonic part of the test section. This leads to a body length of about 1 m (Figure 1). Surface streak patterns are applied in order to align the body parallel to the main flow direction.

2.2. *Flow field visualization technique*

In order to obtain the mean flow characteristics of the base flow region, schlieren flow visualization is used (Figure 2). This technique indicates density gradients in the observed zone. The flow configuration is indicated in Figure 3, obtained from the schlieren photo in Figure 2.[7] The initial boundary layer is fully turbulent; it separates from the model at the edge of the base and is accelerated through the expansion fan. The fan is terminated by the lip shock, which then recompresses the flow to the base pressure. The appearance of the lip shock is due to an overexpansion of the flow at the separation edge. Behind the expansion fan the boundary layer develops as a mixing layer, which is subjected to recompression due to a shock wave and finally forms the wake. The mixing layer encloses the recirculation zone. Further downstream shocks provoked by the wind tunnel geometry appear in the schlieren photograph, but they do not interfere with the near wake.

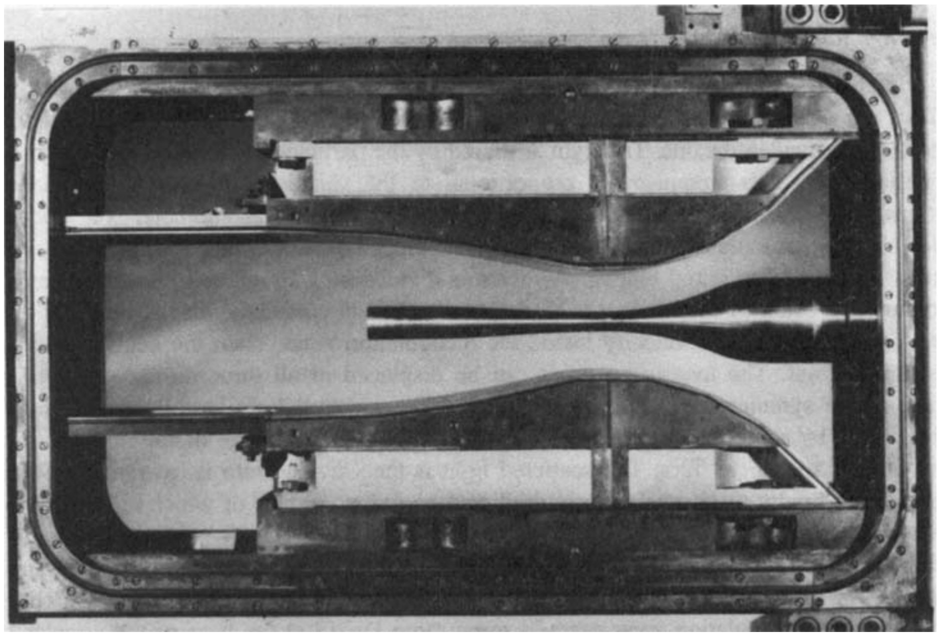

Figure 1. Blow-down tunnel at ISL

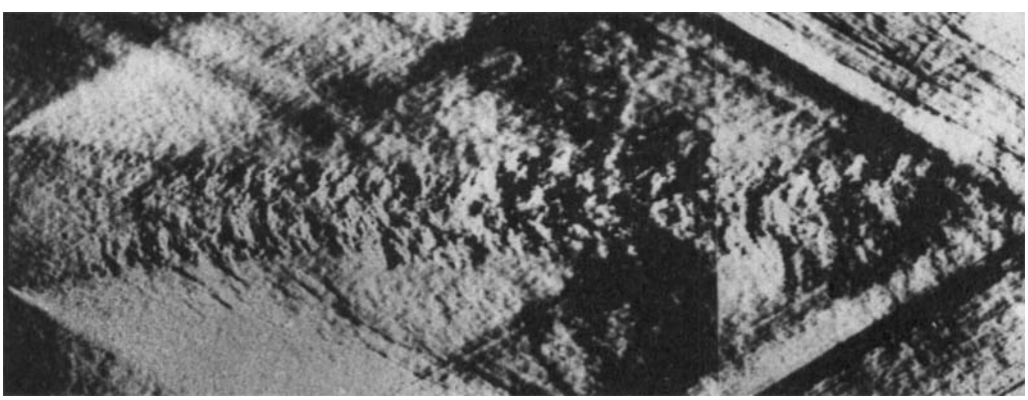

Figure 2. Schlieren flow visualization from near wake[7]

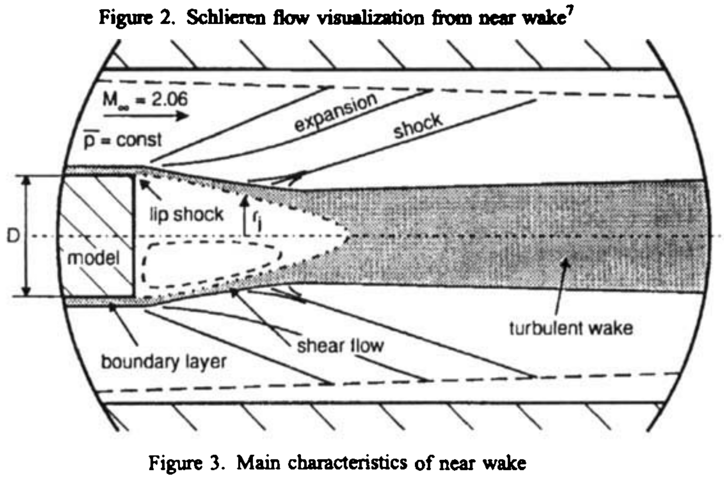

Figure 3. Main characteristics of near wake

2.3. *Investigations with a laser Doppler anemometer*

The principle of laser anemometry is to create an intersection of two laser beams with coherent light. Thus a system of bright and dark plane interference fringes is formed parallel to the bisecting plane of the two incident beams. The light scattered by the particles passing through this intersection varies periodically. This frequency is proportional to the velocity of the particles and inversely proportional to the distance between two fringes. Our laser Doppler anemometer is a four-beam set-up which used two colours of a 5 W argon laser. The green colour can be found at 514·5 nm and the blue one at 488 nm. The initial blue–green beam is divided by a Bragg cell into four beams, two of each colour. One beam of each colour is shifted to 40 MHz to ensure the displacement of the fringes in order to get access to the velocity inside the recirculation zone. Then the beams are focused on the measuring point. The measuring point can be displaced in all three dimensions, but only the velocities in one symmetrical plane are measured. The scattered light is collected in the forward-scattering mode by a convergent optical set-up which focuses the image of the measuring point on the front part of an optical fibre. The scattered light is then divided into its two components. These two light beams finally reach two photomultipliers, the output signals of which are treated by a TSI IFA 750 digital signal processor.

For all these measurements the flow is seeded with DEHS particles introduced in the stilling chamber, just in front of the convergent part that leads to the throat. In order to get a higher density of particles in the recirculation zone, we add some more DEHS at the base of the circular cylinder.

3. DESCRIPTION OF THE NUMERICAL SIMULATION

3.1. *Compressible Navier–Stokes equations*

As already shown in Section 2.1, the case for validation is the wake behind a circular cylinder at $Ma = 2{\cdot}06$. For an axisymmetric co-ordinate system the Navier–Stokes equations governing compressible flows, using mass-averaged variables, may be written in dimensionless form as[8]

$$\frac{\partial q}{\partial t} + \frac{\partial E}{\partial x} + \frac{\partial F}{\partial r} + \frac{F + G}{r} = \frac{1}{Re_{\infty,D}} \left(\frac{\partial E^v}{\partial x} + \frac{\partial F^v}{\partial r} + \frac{F^v + G^v}{r} \right), \tag{1}$$

where q represents the solution vector and E and F are the flux vectors. The appearance of the vector G is provoked by the formulation in cylindrical co-ordinates:

$$q = \begin{pmatrix} \rho \\ \rho u \\ \rho v \\ \rho h \end{pmatrix}, \quad E = \begin{pmatrix} \rho u \\ \rho u^2 + p \\ \rho u v \\ (\rho h + p) u \end{pmatrix}, \quad F = \begin{pmatrix} \rho v \\ \rho u v \\ \rho v^2 + p \\ (\rho h + p) v \end{pmatrix}, \quad G = \begin{pmatrix} 0 \\ 0 \\ -p \\ 0 \end{pmatrix},$$
$$E^v = \begin{pmatrix} 0 \\ \tau_{xx} \\ \tau_{xr} \\ u\tau_{xx} + v\tau_{xr} + \varphi_x \end{pmatrix}, \quad F^v = \begin{pmatrix} 0 \\ \tau_{xr} \\ \tau_{rr} \\ u\tau_{xr} + v\tau_{rr} + \varphi_r \end{pmatrix}, \quad G^v = \begin{pmatrix} 0 \\ 0 \\ -\tau_{\theta\theta} \\ 0 \end{pmatrix}, \tag{2}$$

with the viscous shear stresses τ and heat fluxes φ:

$$\tau_{xx} = 2\mu\frac{\partial u}{\partial x} + \lambda\left(\frac{\partial u}{\partial x} + \frac{1}{r}\frac{\partial}{\partial r}(rv)\right), \qquad \tau_{rr} = 2\mu\frac{\partial v}{\partial r} + \lambda\left(\frac{\partial u}{\partial x} + \frac{1}{r}\frac{\partial}{\partial r}(rv)\right),$$
$$\tau_{\theta\theta} = 2\mu\frac{v}{r} + \lambda\left(\frac{\partial u}{\partial x} + \frac{1}{r}\frac{\partial}{\partial r}(rv)\right), \qquad \tau_{xr} = \mu\left(\frac{\partial u}{\partial r} + \frac{\partial v}{\partial x}\right), \tag{3}$$
$$\varphi_x = \frac{\kappa k_w}{Pr}\frac{\partial T}{\partial x}, \qquad \varphi_r = \frac{\kappa k_w}{Pr}\frac{\partial T}{\partial r}.$$

Here x and r are the co-ordinates and u and v the velocities in the axial and radial directions respectively. The time co-ordinate is called t and ρ, T, p and h represent the density, temperature, pressure and enthalpy respectively. All the dimensionless variables as well as the viscosity coefficient μ, the bulk modulus λ and the thermal conductivity k_w are defined as

$$x = \frac{\bar{x}}{\bar{D}}, \quad r = \frac{\bar{r}}{\bar{D}}, \quad t = \frac{\bar{t}\bar{u}_\infty}{\bar{D}}, \quad u = \frac{\bar{u}}{\bar{u}_\infty}, \quad v = \frac{v}{\bar{u}_\infty} \quad \rho = \frac{\bar{\rho}}{\bar{\rho}_\infty},$$
$$T = \frac{\bar{T}}{\bar{T}_\infty}, \quad p = \frac{\bar{p}}{\bar{\rho}_\infty \bar{u}_\infty^2}, \quad h = \frac{\bar{h}}{\bar{u}_\infty^2}, \quad \mu = \frac{\bar{\mu}}{\bar{\mu}_\infty}, \quad \lambda = \frac{\bar{\lambda}}{\bar{\lambda}_\infty}, \quad k_w = \frac{\bar{k}_w}{\bar{k}_{w\infty}}. \tag{4}$$

The dimensional values are overlined. The index ∞ relates to the unperturbed flow in front of the projectile. The characteristic dimension in our case is the diameter of the cylinder, $\bar{D}$. Therefore the Reynolds number $Re_{\infty,D}$, the Prandtl number Pr and the Mach number Ma_∞ are defined as

$$Re_{\infty,D} = \frac{\bar{\rho}_\infty \bar{u}_\infty \bar{D}}{\bar{\mu}_\infty}, \qquad Pr = \frac{\bar{\mu}_\infty \bar{c}_{p\infty}}{\bar{k}_{w\infty}}, \qquad Ma_\infty = \frac{\bar{u}_\infty}{\bar{c}_\infty}, \tag{5}$$

where $\bar{c} = \surd(\kappa \bar{T}_\infty \bar{R}/\bar{m})$ represents the speed of sound ($\bar{R}$ is the gas constant, $\bar{m}$ is the molar mass and κ is the ratio of the specific heats). The equation set is completed by adding the state equation and, assuming the fluid to be an ideal gas, this yields

$$p\kappa Ma_\infty^2 = \rho T, \tag{6}$$

$$p = [\rho h - \tfrac{1}{2}\rho(u^2 + v^2)](\kappa - 1). \tag{7}$$

Using Stokes' hypothesis, the viscosity coefficient μ_l and the bulk modulus λ are related according to $\lambda = -\frac{2}{3}\mu_l$. Supposing the Prandtl number to be constant, $k_w = \mu_l$ is obtained. The molecular dynamic viscosity μ_l is given by Sutherland's law as

$$\mu_l = T^{3/2}\frac{1 + S_k}{T + S_k}, \tag{8}$$

where the Sutherland constant for air is $S_k = 100\,K/\bar{T}_\infty$.

3.2. *Turbulence model for the near wake*

The effect of turbulence is simulated in terms of an eddy viscosity coefficient μ_t:

$$\mu = \mu_l + \mu_t. \tag{9}$$

In the original Baldwin–Lomax model,[9] which is a two-layer algebraic eddy viscosity model, μ_t is given by

$$\mu_t = \begin{cases} (\mu_t)_{\text{inner}} & \text{for } y \le y_k, \\ (\mu_t)_{\text{outer}} & \text{for } y > y_k, \end{cases} \tag{10}$$

where y represents the normal distance from the wall and y_k is the smallest value of y at which values from the inner and outer formulae are equal. In the inner region the eddy viscosity is given by the Van Driest formulation as

$$(\mu_t)_{\text{inner}} = \rho[K_1 y F_{\text{Dr}}(y)]^2 \left|\frac{\partial u}{\partial y} - \frac{\partial v}{\partial x}\right| Re_{\infty,D}, \tag{11}$$

where $K_1 = 0{\cdot}40$ is the von Kármán constant. The Van Driest damping factor is given by

$$F_{\text{Dr}}(y) = 1 - \exp\left(-\frac{\sqrt{(\rho_w \tau_w y)}}{26\mu_w}\right), \tag{12}$$

where τ_w is the wall shear stress. In the outer region the eddy viscosity coefficient is given by

$$(\mu_t)_{\text{outer}} = \rho K_2 C_{\text{cp}} F_{\text{WAKE}} F_{\text{KLEB}} Re_{\infty,D}, \tag{13}$$

where $K_2 = 0{\cdot}0168$ is Clauser's constant and $C_{\text{cp}} = 1{\cdot}6$ is an additional constant. From the outer function F_{WAKE} we take the smallest value of

$$F_{\text{WAKE}} = \begin{cases} y_{\max} F_{\max}, \\ C_{\text{wk}} y_{\max} u_{\text{Dif}}^2 / F_{\max}, \end{cases} \tag{14}$$

where $u_{\text{Dif}} = \max[\sqrt{(u^2 + v^2)}] - \min[\sqrt{(u^2 + v^2)}]$,

$$F_{\max} = \max\left(y \left|\frac{\partial u}{\partial y} - \frac{\partial v}{\partial x}\right| F_{\text{Dr}}(y)\right) \tag{15}$$

and $y_{\max}$ is the value of y at which $F_{\max}$ occurs. The Klebanoff intermittency correction is given by

$$F_{\text{KLEB}}(y) = \frac{1}{1 + 5{\cdot}5(C_{\text{KLEB}} Y / Y_{\max})^6}, \tag{16}$$

with $C_{\text{KLEB}} = 0{\cdot}3$. To avoid large differences in the behaviour of the normal co-ordinate $y_{\max}$, the average value of four or five neighbouring grid points in the streamwise direction is taken. The comparison between the calculated turbulent intensities and the experimental values has shown large discrepancies in the region of the near wake. Therefore a few modifications of the original turbulence model are necessary.

1. In order to avoid problems in fixing the maximum of $y_{\max}$, the length scale is now measured between the prolongation of the cylinder wall and the line where the velocity is equal to zero. To get a qualitatively correct description of the detachment of the coherent structures near the saddle point, $y_{\max}$ should always be less than $\frac{1}{3}\bar{D}$ (Figure 4).
2. For the outer function F_{WAKE} we can write

$$F_{\text{NEARW}} = C_{\text{NEARW}} C_{\text{wk}} y_{\max} \frac{u_{\text{Dif}}^2}{F_{\max}}, \tag{17}$$

where $C_{\text{NEARW}} = 2$.

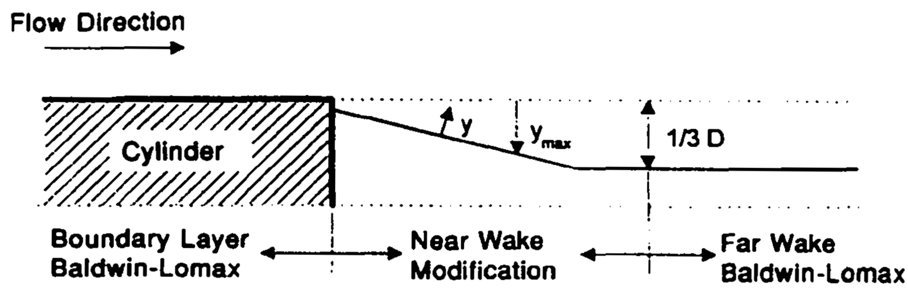

Figure 4. Domains of turbulence models

3. The value y' is now the distance between the point y and the line where the velocity is equal to zero. F_{max} is the maximum of

$$F_{max(y')} = \max|y'| \left|\frac{\partial u}{\partial y} - \frac{\partial v}{\partial x}\right|. \tag{18}$$

4. The Klebanoff intermittency function is replaced by a normal distribution, assuming that the derivative at the point of deflection is equal to the maximum vorticity in the wake:

$$F_{Gauss} = \exp\left(-\frac{e}{2}\left|\frac{\partial u}{\partial y} - \frac{\partial v}{\partial x}\right|^2 (y')^2\right). \tag{19}$$

If the determined eddy viscosity of the Baldwin–Lomax model is greater than the near-wake viscosity, the original turbulence model is used again.

3.3. *Weighted residual approximation*

With a node-centred scheme, problems can be expected for equations (1) when r is equal to zero. In order to avoid these problems we multiply the system by r:

$$\frac{\partial rq}{\partial t} + \frac{\partial rE}{\partial x} + \frac{\partial rF}{\partial r} + G = \frac{1}{Re_{\infty,D}}\left(\frac{\partial rE^v}{\partial x} + \frac{\partial rF^v}{\partial r} + G^v\right). \tag{20}$$

A time-stepping scheme for the solution of this equation can be produced by writing a Taylor series in time, correct to second order, as

$$rq^{n+1} = rq^n + \Delta t\frac{\partial rq^n}{\partial t} + \frac{\Delta t^2}{2}\frac{\partial^2 rq^n}{\partial t^2} + \cdots. \tag{21}$$

The time derivatives may be evaluated in terms of space derivatives in the Lax–Wendroff[10] fashion. $A = \partial rE/\partial rq$, $B = \partial xF/\partial rq$ and $C = \partial G/\partial rq$ are the Jacobi matrices for the Euler equations. Viscous terms involving derivatives or products of derivatives are treated in the following manner.[11,12]

$$\begin{aligned} rE^v &= rU_1\left(rq, \frac{\partial rq}{\partial x}\right) + rU_2\left(rq, \frac{\partial rq}{\partial r}\right), \\ rF^v &= rW_1\left(rq, \frac{\partial rq}{\partial x}\right) + rW_2\left(rq, \frac{\partial rq}{\partial r}\right), \end{aligned} \tag{22}$$

where $A^v_x = \partial rU_1/\partial rq$, $AD^v_x = (\partial/\partial x)\partial rU_1/\partial rq$, $A^v_r = \partial rU_2/\partial rq$, $AD^v_r = (\partial/\partial r)\partial rU_2/\partial rq$, $B^v_x = \partial rW_1/\partial rq$, $BD^v_x = (\partial/\partial x)\partial rW_1/\partial rq$, $B^v_r = \partial rW_2/\partial rq$ and $BD^v_r = (\partial/\partial r)\partial rW_2/\partial rq$. Thus we obtain

$$\begin{aligned}\frac{\partial rE^v}{\partial x} &= A^v_x\frac{\partial rq}{\partial x} + AD^v_x\frac{\partial}{\partial x}\frac{\partial rq}{\partial x} + A^v_r\frac{\partial rq}{\partial r} + AD^v_r\frac{\partial}{\partial x}\frac{\partial rq}{\partial r},\\ \frac{\partial rF^v}{\partial r} &= B^v_x\frac{\partial rq}{\partial r} + BD^v_x\frac{\partial}{\partial r}\frac{\partial rq}{\partial x} + B^v_r\frac{\partial rq}{\partial r} + BD^v_r\frac{\partial}{\partial r}\frac{\partial rq}{\partial r}.\end{aligned} \tag{23}$$

For the derivatives of second order we make the following transformation, for example:

$$AD^v_x\frac{\partial}{\partial x}\frac{\partial rq}{\partial x} = \frac{\partial}{\partial x}\left(AD^v_x\frac{\partial rq}{\partial x}\right) - AD^v_{x,x}\frac{\partial rq}{\partial x}, \tag{24}$$

where subscripts x and r represent the derivatives of the Jacobi matrices in the corresponding directions. The matrices could be arranged in the following way:

$$\begin{aligned} AV_x\frac{\partial rq}{\partial x} &= (A^v_x - AD^v_{x,x})\frac{\partial rq}{\partial x}, & AV_r\frac{\partial rq}{\partial r} &= (A^v_r - AD^v_{r,x})\frac{\partial rq}{\partial r},\\ BV_x\frac{\partial rq}{\partial x} &= (B^v_x - BD^v_{x,r})\frac{\partial rq}{\partial x}, & BV_r\frac{\partial rq}{\partial r} &= (B^v_r - BD^v_{r,r})\frac{\partial rq}{\partial r},\end{aligned} \tag{25}$$

where AV_x is equal to zero. All matrices are described in the Appendix. Applying the divergence theorem, the Galerkin weighted residual statement, as shown by Löhner *et al.*[4] and Peraire *et al.*,[5] can be expressed as

$$\int_\Omega \Delta rqN\,\mathrm{d}\Omega = f_\Omega + f_\Gamma, \tag{26}$$

where N is a piecewise linear approximation. By using the same approximation for the radius r, a higher accuracy in the radial direction is obtained,[13] which permits us to calculate the pressure, enthalpy, etc. on the axis. The integrals that appear in the mass matrix, $\int_r\int_x 2\pi N_jN_ir_iN_kq^{n+1}_k\,\mathrm{d}x\,\mathrm{d}r$, are more difficult to evaluate; however, they may still be derived in closed form. The approximation for the solution vector q is linear and for the Jacobi matrices it is piecewise constant. Thus no loss of accuracy can be noted, because the matrices contain derivatives of the vector q, which will be piecewise constant.

3.4. *Time step and artificial viscosity*

With this approximation scheme we get a consistent mass matrix, the entries of which are defined by

$$\mathbf{M} = \int_r\int_x N_jN_ir_iN_k\,\mathrm{d}x\,\mathrm{d}r. \tag{27}$$

This equation system is solved explicitly and iteratively[14] by writing

$$\Delta rq^{(m)} = f_\Omega + f_\Gamma + \Delta rq^{(m-1)} - \mathbf{M}\mathbf{M}_\mathrm{L}^{-1}\Delta rq^{(m-1)}, \tag{28}$$

where superscript (m) represents the mth iteration, $\Delta rq^{(0)} = 0$ and $\mathbf{M}_\mathrm{L}$ is the lumped mass matrix $(\mathbf{M}_\mathrm{L})_{jj} = \sum_{k=1}^{n_{el}}(\mathbf{M})_{jk}$. In order to comply with the stability condition, the local time step should satisfy the relation[15]

$$\Delta t < \frac{1}{6}\frac{R^2_{el}}{\mu}, \tag{29}$$

where R_{el} is the radius of the inscribed circle. Owing to shocks and other discontinuities inherent in this problem, further stabilization is necessary. For the boundary layer we use the artificial viscosity

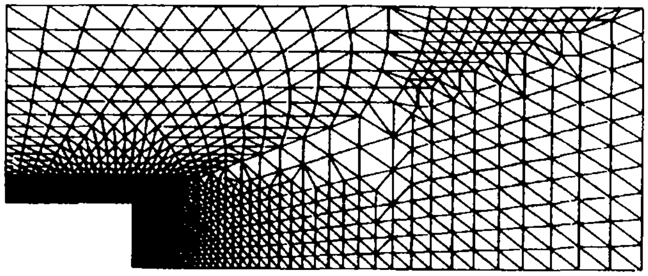

Figure 5. Initial grid for near wake with 2748 elements and 1453 nodes

proposed by MacCormack and Baldwin[16] and Morgan and Peraire:[17] elsewhere the method suggested by Lapidus[18] and Löhner *et al.*[19] is applied.

4. MESH DESCRIPTION

The mesh is defined within the boundaries given by our validation experiment. The velocities at the inflow boundary, which is situated one diameter before the base, are given by the investigations with the laser Doppler anemometer. The upper wall is treated as a solid wall without any viscous effects. The outflow boundary is set far downstream to ensure that there are only supersonic velocities. Between the wall and the flow boundaries several different meshes have been generated for this configuration. The initial grid is built up in two steps with the so-called Delaunay triangulation.[20] First a set of nodes in the computational domain is generated, then the elements are calculated from the node co-ordinates. The Delaunay triangulation is an algorithm allowing one to find well-adapted triangles (small interior angles are avoided) associated with the set of given nodes.[21,22] The initial mesh has 21 nodes at the inflow boundary and 25 nodes on the cylinder wall. The relatively coarse initial grid, which covers the entire investigation domain, is successively refined by subdividing elements into smaller elements. In this case a triangle is divided into four subtriangles. The boundary layer and the zone just behind the base (special consideration being given to the lip shock) are refined (Figure 5). The mesh with which the numerical simulation was started has 2748 elements and 1453 nodes. If the solution converges, the grid is refined until there are no marked differences left between two successive grids. The last mesh contains 25,412 elements and 13,062 nodes.

5. COMPARISON BETWEEN MEASUREMENT AND SIMULATION

Plate 1 represents the calculated density contribution and velocities in the near wake. The position of the calculated shocks and expansion waves is identical with the schlieren flow visualization. Even the contours of the recirculation zone are the same. The general features of the flow field are well represented from a qualitative point of view. In Plate 2 the absolute values of the mean velocities are compared with the measured ones. In fact, as it appears near the centreline, the values of the reverse axial velocities are overpredicted and the reacceleration after the reattachment point is higher in the experiment. Moreover, the turbulence level (Plate 3), represented by the Reynolds shear stress values, is underpredicted behind the saddle point. There are three reasons for this behaviour. In order to increase the data rate of the laser Doppler measurements, some particles have to be added near the base. Therefore the turbulent intensities are not measured in this region and the reverse axial velocities may be too low. In the schlieren photograph a detachment of coherent structures could be seen near the reattachment point. The flow is no longer axisymmetric, therefore three-dimensional effects are

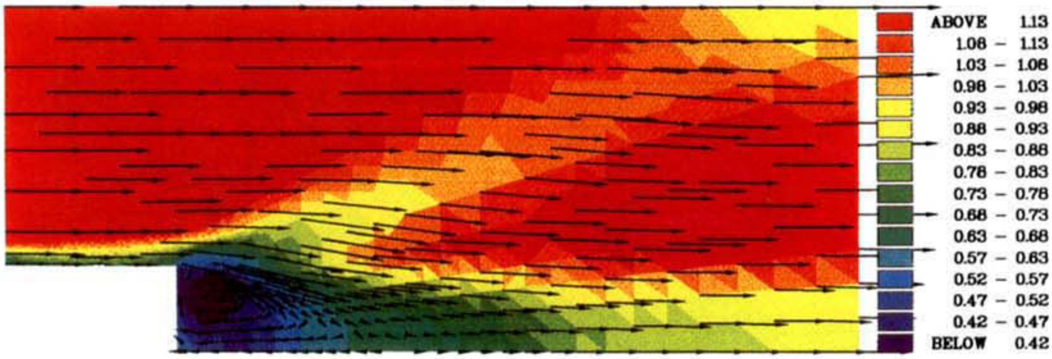

Plate 1. Density contribution and velocities in the near wake

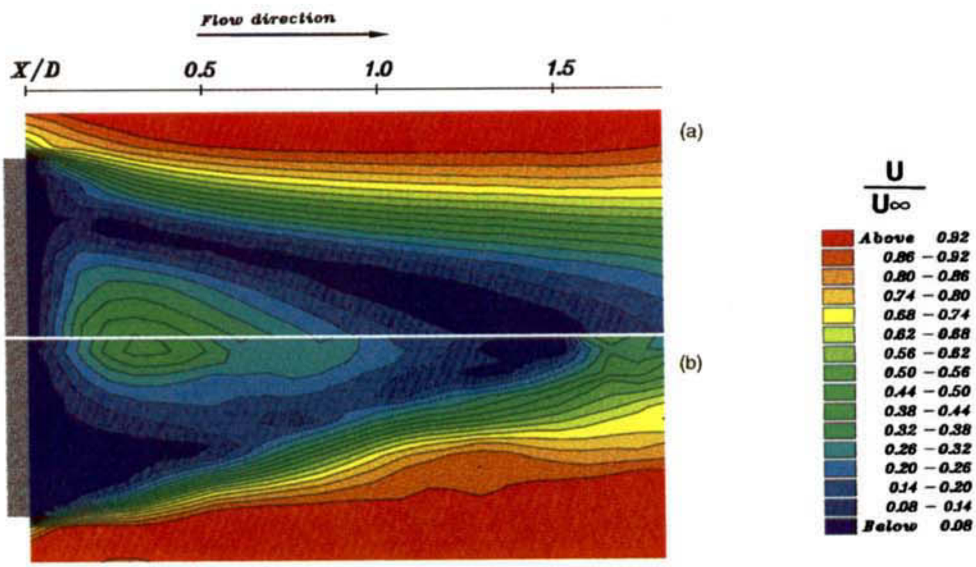

Plate 2. Comparison of the velocity contribution. (a) simulation, (b) experiment

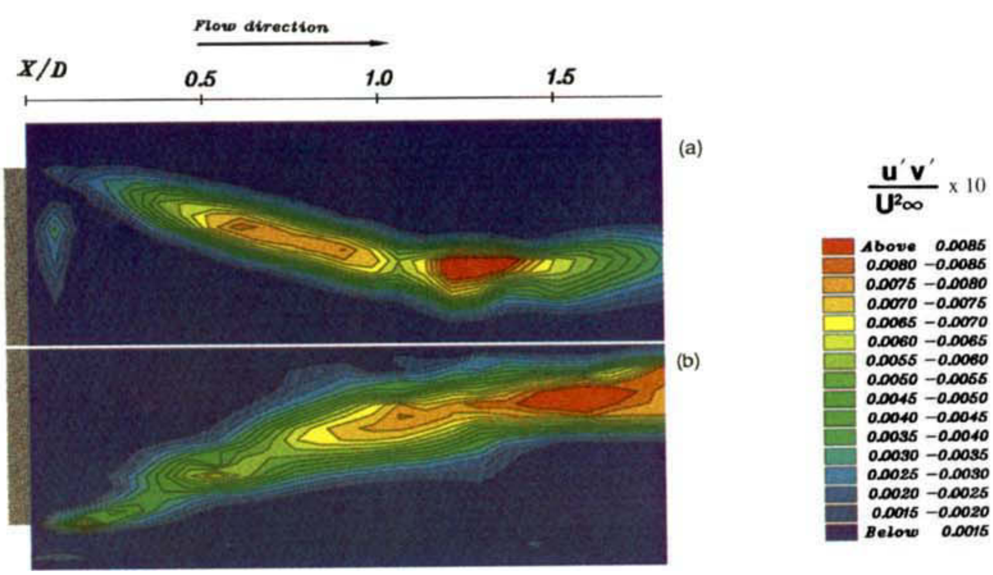

Plate 3. Comparison of the Reynolds shear stress contribution. (a) simulation, (b) experiment

prevailing. It is important to keep in mind that we calculate a 'quasi-steady' solution, but actually the flow is unsteady.[23] Therefore effects provoked by the detachment of the coherent structures could not be shown by these numerical investigations.

6. CONCLUSIONS

The prediction of the numerical simulation has shown that although the modified algebraic turbulence model uses simplified approaches, the solution leads to a quantitatively correct description of the near-wake properties. However, these results are only obtained by a modification of the original turbulence model. Numerical investigations have to be compared with experimental values in order to show the reliability of these methods. Only with this intermediate step of validation will numerical methods gain more importance in the development of aerospace technologies.

ACKNOWLEDGEMENTS

The author is grateful to Professor Dr.-Ing H. Oertel and Dr.-Ing. E. Laurien for their valuable comments, suggestions and assistance throughout this work.

APPENDIX: JACOBI MATRICES

A-matrix: $A = \partial rE/\partial rq$

$$\begin{bmatrix} 0 & 1 & 0 & 0 \\ \frac{\kappa-3}{2}u^2 + \frac{\kappa-1}{2}v^2 & (3-\kappa)u & (1-\kappa)v & \kappa-1 \\ -uv & v & u & 0 \\ -\kappa hu + (\kappa-1)u(u^2+v^2) & \kappa h + \frac{1-\kappa}{2}(3u^2+v^2) & (1-\kappa)uv & \kappa u \end{bmatrix}. \tag{30}$$

B-matrix: $B = \partial rF/\partial rq$

$$\begin{bmatrix} 0 & 0 & 1 & 0 \\ -uv & v & u & 0 \\ \frac{\kappa-3}{2}v^2 + \frac{\kappa-1}{2}u^2 & (1-\kappa)u & (3-\kappa)v & \kappa-1 \\ -\kappa hv + (\kappa-1)v(u^2+v^2) & (1-\kappa)vu & \kappa h + \frac{1-\kappa}{2}(u^2+3v^2) & \kappa v \end{bmatrix}. \tag{31}$$

C-matrix: $C = \partial G/\partial rq$

$$\begin{bmatrix} 0 & 0 & 0 & 0 \\ 0 & 0 & 0 & 0 \\ \frac{1-\kappa}{2r}(u^2+v^2) & \frac{\kappa-1}{r}u & \frac{\kappa-1}{r}v & \frac{1-\kappa}{r} \\ 0 & 0 & 0 & 0 \end{bmatrix}. \tag{32}$$

AD_x^{v}-matrix: $AD_x^{\mathrm{v}} = \partial r V_1/\partial r q_x$

$$\begin{bmatrix} 0 & 0 & 0 & 0 \\ -(2\mu+\lambda)\dfrac{u}{\rho} & (2\mu+\lambda)\dfrac{1}{\rho} & 0 & 0 \\ -\mu\dfrac{v}{\rho} & 0 & \mu\dfrac{1}{\rho} & 0 \\ -(2\mu+\lambda)\dfrac{u^2}{\rho} - \mu\dfrac{v^2}{\rho} - \dfrac{\kappa k_{\mathrm{w}}}{Pr_\infty}\dfrac{h-u^2-v^2}{\rho} & (2\mu+\lambda)\dfrac{u}{\rho} - \dfrac{\kappa k_{\mathrm{w}}}{Pr_\infty}\dfrac{u}{\rho} & \mu\dfrac{v}{\rho} - \dfrac{\kappa k_{\mathrm{w}}}{Pr_\infty}\dfrac{v}{\rho} & \dfrac{\kappa k_{\mathrm{w}}}{Pr_\infty}\dfrac{1}{\rho} \end{bmatrix}. \tag{33}$$

AD_r^{v}-matrix: $AD_r^{\mathrm{v}} = \partial r V_2/\partial r q_r$, BD_x^{v}-matrix: $BD_x^{\mathrm{v}} = \partial r W_1/\partial r q_x$

$$\begin{bmatrix} 0 & 0 & 0 & 0 \\ -\lambda\dfrac{v}{\rho} & 0 & \lambda\dfrac{1}{\rho} & 0 \\ -\mu\dfrac{u}{\rho} & \mu\dfrac{1}{\rho} & 0 & 0 \\ -(\lambda+\mu)\dfrac{uv}{\rho} & \mu\dfrac{v}{\rho} & \lambda\dfrac{u}{\rho} & 0 \end{bmatrix}, \quad \begin{bmatrix} 0 & 0 & 0 & 0 \\ -\mu\dfrac{v}{\rho} & 0 & \mu\dfrac{1}{\rho} & 0 \\ -\lambda\dfrac{u}{\rho} & \lambda\dfrac{1}{\rho} & 0 & 0 \\ -(\lambda+\mu)\dfrac{uv}{\rho} & \lambda\dfrac{v}{\rho} & \mu\dfrac{u}{\rho} & 0 \end{bmatrix}. \tag{34}$$

BD_r^{v}-matrix: $BD_r^{\mathrm{v}} = \partial r W_2/\partial r U$

$$\begin{bmatrix} 0 & 0 & 0 & 0 \\ -\mu\dfrac{u}{\rho} & \mu\dfrac{1}{\rho} & 0 & 0 \\ -(2\mu+\lambda)\dfrac{v}{\rho} & 0 & (2\mu+\lambda)\dfrac{1}{\rho} & 0 \\ -(2\mu+\lambda)\dfrac{v^2}{\rho} - \mu\dfrac{u^2}{\rho} - \dfrac{\kappa k_{\mathrm{w}}}{Pr_\infty}\dfrac{h-u^2-v^2}{\rho} & \mu\dfrac{u}{\rho} - \dfrac{\kappa k_{\mathrm{w}}}{Pr_\infty}\dfrac{u}{\rho} & (2\mu+\lambda)\dfrac{v}{\rho} - \dfrac{\kappa k_{\mathrm{w}}}{Pr_\infty}\dfrac{v}{\rho} & \dfrac{\kappa k_{\mathrm{w}}}{Pr_\infty}\dfrac{1}{\rho} \end{bmatrix}. \tag{35}$$

AV_r-matrix: $AV_r = A_r^{\mathrm{v}} - AD_{r,r}^{\mathrm{v}}$

$$\begin{bmatrix} 0 & 0 & 0 & 0 \\ 0 & 0 & 0 & 0 \\ \mu\dfrac{u}{r\rho} & -\mu\dfrac{1}{r\rho} & 0 & 0 \\ (\lambda-\mu)\left(\dfrac{v}{r\rho^2}\dfrac{\partial r\rho u}{\partial r} - \dfrac{u}{r\rho^2}\dfrac{\partial r\rho v}{\partial r}\right) - (\lambda-\mu)\dfrac{uv}{r\rho} & (\lambda-\mu)\left(\dfrac{1}{r\rho^2}\dfrac{\partial r\rho v}{\partial r} - \dfrac{v}{r\rho^2}\dfrac{\partial r\rho}{\partial r}\right) + (\lambda-\mu)\dfrac{v}{r\rho} & (\lambda-\mu)\left(\dfrac{u}{r\rho^2}\dfrac{\partial r\rho}{\partial r} - \dfrac{1}{r\rho^2}\dfrac{\partial r\rho u}{\partial r}\right) & 0 \end{bmatrix}. \tag{36}$$

BV_x-matrix: $BV_x = B_x^{\mathrm{v}} - BD_{x,x}^{\mathrm{v}}$

$$\begin{bmatrix} 0 & 0 & 0 & 0 \\ 0 & 0 & 0 & 0 \\ 0 & 0 & 0 & 0 \\ (\mu-\lambda)\left(\dfrac{v}{r\rho^2}\dfrac{\partial r\rho u}{\partial x} - \dfrac{u}{r\rho^2}\dfrac{\partial r\rho v}{\partial x}\right) & (\mu-\lambda)\left(\dfrac{1}{r\rho^2}\dfrac{\partial r\rho v}{\partial x} - \dfrac{v}{r\rho^2}\dfrac{\partial r\rho}{\partial x}\right) & (\mu-\lambda)\left(\dfrac{u}{r\rho^2}\dfrac{\partial r\rho}{\partial x} - \dfrac{1}{r\rho^2}\dfrac{\partial r\rho u}{\partial x}\right) & 0 \end{bmatrix}. \tag{37}$$

BV_r-matrix: $BV_r = B_r^v - BD_{r,r}^v$

$$\begin{bmatrix} 0 & 0 & 0 & 0 \\ \mu\dfrac{u}{r\rho} & -\mu\dfrac{1}{r\rho} & 0 & 0 \\ 2\mu\dfrac{v}{r\rho} & 0 & -2\mu\dfrac{1}{r\rho} & 0 \\ \left(\mu-\dfrac{\kappa k_w}{Pr_\infty}\right)\dfrac{u^2}{r\rho}+\dfrac{\kappa k_w}{Pr_\infty}\dfrac{h}{r\rho}\left(2\mu-\lambda-\dfrac{\kappa k_w}{Pr_\infty}\right)\dfrac{v^2}{r\rho} & \left(\dfrac{\kappa k_w}{Pr_\infty}-\mu\right)\dfrac{u}{r\rho} & \left(\dfrac{\kappa k_w}{Pr_\infty}-2\mu+\lambda\right)\dfrac{v}{r\rho} & -\dfrac{\kappa k_w}{Pr_\infty}\dfrac{1}{r\rho} \end{bmatrix}. \tag{38}$$

REFERENCES

1. J. Delery and B. Wagner, 'Results on Garteur Action Group AG09' *Flow past Missiles Afterbodies, AGARD CP-493*, 1990.
2. J. Delery and R. G. Lacau, 'Prediction of base-flow', *Special Course on Missile Aerodynamics, AGARD R-754*, 1988, pp. g.1–g.12.
3. H. Oertel, 'Validation of Navier–Stokes methods for aerospace application', *Proc. ISCFD Con.*, 1989.
4. R. Löhner, K. Morgan and O. C. Zienkiewicz, 'The solution of non-linear hyperbolic equation systems by the finite element method', *Int. j. numer. methods fluids*, **4**, 1043–1063 (1984).
5. J. Peraire, J. Peiro, L. Formaggia, K. Morgan and O. C. Zienkiewicz, 'Finite element Euler computations in 3D', *Int. j. numer. methods eng.*, **26**, 2135–2159 (1988).
6. J. Zierep, *Theoretische Gasdynamik*, Braun, Karlsruhe, 1976.
7. R. Niessen, 'Speckle-optische Messungen räumlicher Strukturen in einer turbulenten, kompressiblen Nachlaufströmung', *ISL-R 101/94*, 1994.
8. B. Mueller, 'Berechnung abgelöster laminarer Überschallströmungen um nichtangestellte stumpfe Rotationskörper', *DFVLR-FB 78-30*, 1985.
9. B. Baldwin and H. Lomax, 'Thin layer approximation and algebraic model for separated turbulent flows', *AIAA Paper 78-257*, 1978.
10. P. D. Lax and B. Wendroff, 'Difference schemes for hyperbolic equations with high order of accuracy', *Commun. Pure Appl. Math.*, **17**, 381–398 (1964).
11. R. M. Beam and R. F. Warming, 'An implicit factored scheme for the compressible Navier–Stokes equations', *AIAA J.*, **16**, 393–402 (1978).
12. O. Hassan, K. Morgan and J. Peraire, 'An implicit finite element method for the high speed flows', *Int. j. numer. methods eng.*, **32**, 183–205 (1991).
13. R. Löhner, J. D. Baum, E. Loth and R. Ramamurti, 'A finite element solver for axisymmetric compressible flows', *AIAA Paper 89-1794*, 1989.
14. J. Donea and S. Giuliani, 'A simple method to generate high order accurate convection operators for explicit schemes based on linear finite elements', *Int. j. numer. methods fluids*, **1**, 63–79 (1981).
15. E. Laurien, M. Böhle, H. Holthoff and J. M. Odendahl, 'Stability and convergence of the Taylor–Galerkin finite element method for the Navier–Stokes equations', *ZAMM*, **71**, T411–T413 (1991).
16. R. W. MacCormack and B. S. Baldwin, 'A numerical method for solving the Navier–Stokes equations with application to the shock boundary interactions', *AIAA Paper 75-1*, 1975.
17. K. Morgan and J. Peraire, 'Finite element methods for compressible flows', *VKI Lecture Series, Computational Fluid Dynamics, 1987-04*, 1987.
18. A. Lapidus, 'A detached shock calculation by second-order finite differences', *J. Comput. Phys.*, **2**, 154–177 (1967).
19. R. Löhner, K. Morgan and J. Peraire, 'A simple extension to multi-dimensional problems of the artificial viscosity due to Lapidus', *Commun. Appl. Numer. Methods*, **1**, 141–147 (1985).
20. S. W. Sloan and G. T. Houlsby, 'An implementation of Watson's algorithm for computing two-dimensional Delaunay triangulations', *Adv. Eng. Softw.*, **6**, 192–196 (1984).
21. E. Laurien, 'Application of finite element methods to the computation of external flows', *Space Course*, Aachen, 1991.
22. N. P. Weathill and J. A. Shaw, 'Component adaptive grid generation for aircraft configurations', *Three dimensional grid generation for complex configurations: Recent Progress, AGARD-AG-309*, 1988.
23. F. Leopold, 'Simulation und stabilitätstheoretische Untersuchungen zum kompressiblen Nachlauf eines längsangeströmten Kreiszylinders', *ZLR 93-5*, 1993.